TECHNICAL PAPER

An analytical method to design annular microfilaments with uniform temperature

Ferenc Bíró[1] · András Deák[1] · István Bársony[1] · Nikolay Samotev[2] · Csaba Dücső[1]

Abstract

Due to their complex electro-thermal characteristics microhotplates used in environmental gas sensors require careful design to exhibit uniform temperature and low power dissipation during the expected long time operation. The layout design becomes more complex if the multiple operational parameters required by the battery operation and the driver and readout logic are considered. In this paper, we describe a simple analytical filament design procedure to determine the dimensions of the annular metal filament exhibiting uniform surface temperature without additional heat distribution layer. The presented method operates with the cumulative thermal losses towards the ambient and heat conduction via the membrane. Moreover, it handles the operation requirements like the targeted temperature in the atmospheric environment, supply voltage range, current density, filament layer thickness and its coverage ratio. The efficacy of the method is demonstrated by electrical and thermal characterisation of the manufactured devices having 150 μm diameter active area. The microheater achieves the targeted 500 °C operation temperature with 1.4–1.55 V supply. The temperature non-uniformity along the filament was measured by Spectral pyrometry and was found to decrease from ± 3.5% to ± 1% when the temperature was raised from 530 to 830 °C.

1 Introduction

Microheaters or microhotplates are used to provide the necessary elevated temperature to facilitate sensing, radiation or to get the moving parts into action. The main component of these devices is a micromachined membrane suspending a heater filament in its centre. Although the first silicon technology compatible microheaters appeared in the late 80s (Nuscheler 1986), still play important role in today's commercial electronics and scientific instruments, such as in gas sensors (Rüffer et al. 2018; White 2014; Yunusa et al. 2014), in flow- and accelerometers (Kuo et al. 2012), in actuators (Ishaku et al. 2021; vanHorn and Zhou 2016), in IR sources (Popa and Udrea 2019; Ishihara et al. 2017; Lochbaum et al. 2017), in nano-calorimeters (Hartman et al. 2021; Mele et al. 2016; Queen and Hellman

2009), and are used in studying of heat transfer properties of materials (Marconot et al. 2021). During the last decades many different filament designs were fabricated on full or perforated membranes or in cantilever form (Lee and King 2007), on a large variety of substrate materials, such as ceramics (Roslyakov et al. 2021), glass (Vauchier et al. 1991), gallium-arsenide (Hotovy et al. 2008) and silicon (Graf et al. 2007; Hierlemann 2005).

The reduced power dissipation microheaters designed for calorimetric and chemoresistive gas sensing are suspended by thermally insulating membranes to meet the essential thermal and electrical requirements, e.g. the temperature uniformity inside their active area, device size, power dissipation, supply voltage range, filament current density, etc.

In view of the required temperature uniformity the rather symmetric, circular shaped active area (often called heated area) designs are preferred (Graf et al. 2007, p. 30). Due to the complex nature of the electro-thermal phenomena present during operation, it is almost impossible to consider all the physical effects in the filament design. Therefore, Finite Element Method (FEM) assisted design strategies and various models have been built which were able to provide accurate temperature profiles for the filament

✉ Ferenc Bíró
biro.ferenc@ek-cer.hu

1 Centre for Energy Research, Konkoly-Thege Miklós út 29-33, 1121 Budapest, Hungary

2 National Research Nuclear University MEPhI (Moscow Engineering Physics Institute), Kashirskoe Highway 31, Moscow 115409, Russian Federation

optimisation (Graf et al. 2007, pp. 17–28; Khan and Falconi 2013). The issue of the filament temperature uniformity was raised in the early works presenting the first gas sensor platforms (Dibbern 1990; Gall 1991; Hille and Strack 1992). Among the different approaches to achieve it was the application of a heat spreading layer which introduces a thin metal film or silicon over the heated area (Briand et al. 2000). Another suggested solution introduced an additional heater ring around the active area to supply the heat lost via the supporting membrane (Hille and Strack 1992).

Khan and co-workers presented an effective model for circular symmetric microhotplates to calculate the temperature profile of the heated area (Khan and Falconi 2014). Based on similar thermal management strategy and FEM assisted design procedure, a 75 μm radius circular shaped microfilament was optimised with improved temperature uniformity by Ali et al. (2009). The filament system of the fabricated device was divided into outer and inner ring heaters. Furthermore, it comprised a silicon heat spreading layer to improve the temperature uniformity. After optimisation the microheater at around 300 °C showed temperature non-uniformity within 2%.

Another concept to improve the temperature uniformity of serpentine and spiral heaters by changing filament geometries was proposed by Wu et al. (2019). Exploiting the FEM assisted design procedure improved temperature homogeneity was achieved with high coverage ratio.

The complex FEM thermal analysis procedures can predict the temperature distribution of the microheater, and the physical quantities can be extracted from the model of a given filament layout for further device optimisation. Nevertheless, it is still hard to describe how to achieve the optimum layout and device structure to meet the operational requirements beyond the temperature uniformity.

In this work we present a simplified analytical method to facilitate the design of annular single filament suspended on full membrane. Our approach helps to calculate the heater dimensions of the outer and inner rings to achieve uniform operation temperature and set the supply voltage range. In view of the degradation phenomena this calculation also takes into account the filament layer thicknesses and the current density limitations while maintaining the uniform temperature (as limited by the error of the local temperature measurement) with the highest coverage ratio.

2 Essential parameters

2.1 Microheater topology

The basic concept of the filament and microheater topology is illustrated in Fig. 1. The microheater is divided into three
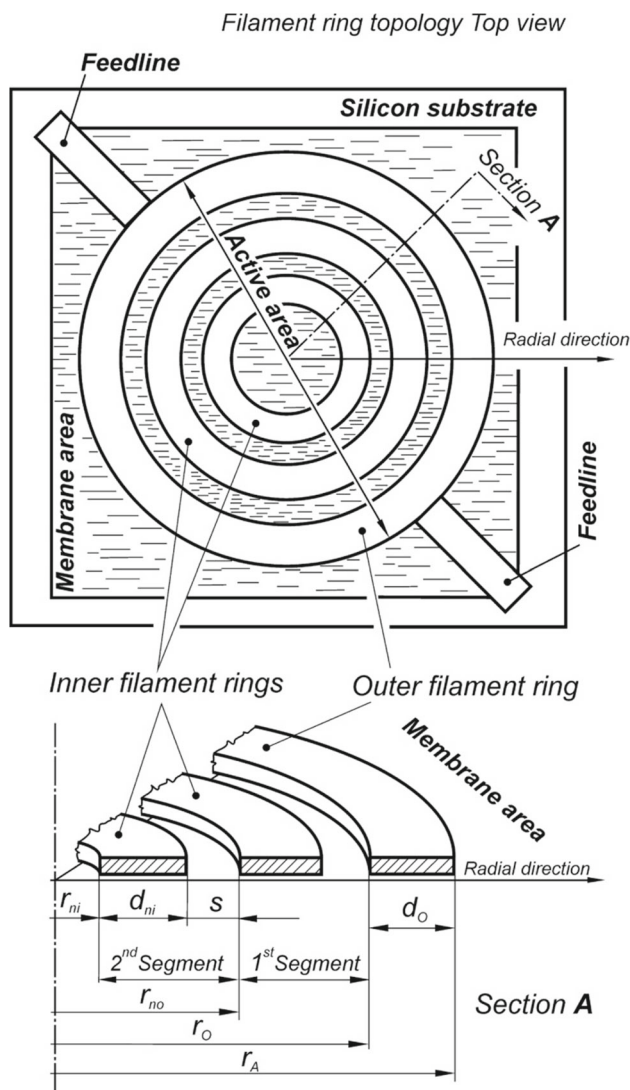

Fig. 1 Topology of the microheater and the filament ring architecture used in the present design procedure to define the main parts of the microheater and their dimensions. In the top view the membrane is hatched, whereas the filament rings on it are clear. The active area is bordered by the outer perimeter of the outer ring. The interior of the active area is divided into the outer ring and actually two segments of the inner rings. Each segment domain comprises a filament ring and an insulation spacing (*s*) as indicated in the cross-section. Section A represents the dimensions of inner and outer rings, as well as the dimensions of segments

main parts: (i) The active area with the circular filament (ii) membrane area and (iii) feedlines.

(i) The annular filament topology is considered in the active area. The filament is split into one outer ring and inner rings. Every ring is isolated with insulation spacing (*s*). Every segment comprises a ring and insulation spacing.

(ii) In the full membrane device we call the membrane area between the outer perimeter of the outer ring and the substrate.

(iii) The filament is powered through the feedlines.

The filament design considers the following conditions:

– Microheater operates in steady-state conditions: design method assumes that, during the operation of the microheater all of the physical parameters which can affect the temperature of the active area, i.e. supply voltage, ambient temperature, pressure, gas composition, etc. are unchanged in time.

– Microheater operates under ambient pressure and temperature: pressure and temperature of the gaseous media around the microheater has effect on the temperature of the active area through the convective heat transport. For example a lower ambient pressure decreases the magnitude of the convective heat transport and changes the temperature-heating power characteristics of the microheater. Because, the microheater is primarily designed for air quality sensor platforms, ambient pressure and temperature values were considered.

– The filament material is not degrading and the effect of mechanical stress is negligible: metal thin films are widely applied to form the filaments of microheaters. Filaments may have specific geometries and are loaded with different magnitude of current density. Under operation the constant electron flow induces atom migration in the conductor and resulting material deficiencies at specific regions along the filament and changes its local and total resistance. Mechanical stress also affects the magnitude of material constants i.e. temperature coefficient of resistance, specific electrical resistance. Effects of these phenomena were ignored in the design.

– The same I direct current flows in every ring and feedline: because, the filament layout is created by the series connection of the filament sections, the same heater current flow in each sections. So, the same I current must be considered in rings and feedlines during the design process.

– All the filament rings are at the same operation temperature T: this assumption is support the temperature uniformity. When the filament ring temperatures are not equal lateral heat transfer effects are present, and hotspots can appear in the system making the calculations more complex.

– Only Joule heat is present: when microheaters are operated as sensor platforms the active area is covered with sensing layer. The heat generated by a chemical reaction or physical phase transformation in the sensing layer acts as an extra heat source and changes the thermal state of the active area. In this design method the effect of these layers or coatings are not considered.

In Fig. 1 definition of notations are the following:

r_A outer radius of the outer ring
r_O inner radius of the outer ring
d_O width of the outer ring
r_{no} outer radius of the nth segment
r_{ni} inner radius of the nth segment
d_{ni} width of the nth inner filament ring

The index "n" denotes both the order of the segment and of the ring which is running therein.

2.2 Power balances

Power balances and thermal loss effects are discussed for active area of uniform temperature (Fig. 2). To maintain the uniform temperature along the filament, the electric power consumption for any given area must be equal with the sum of the heat losses of that area at temperature T, as illustrated in the top of Fig. 2. Consistent with our assumption that the temperature of the active area is uniform, there is no lateral heat transfer between the interior parts of the heated area (Hille and Strack 1992). Thereby, only the surface related thermal losses terms need to be
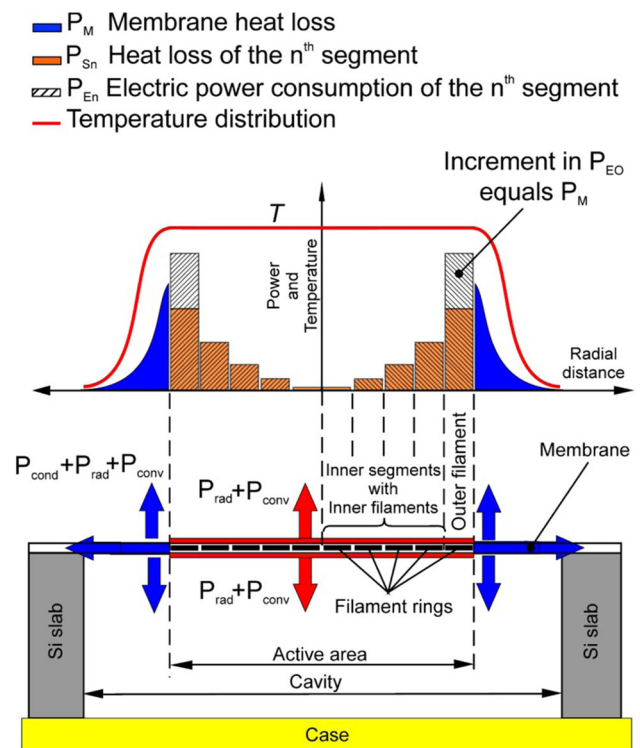

Fig. 2 Illustration of the power balance and the thermal loss phenomena present at full membrane microheater with annular filament arrangement at uniform temperature in the active area. In the bottom drawing the cross section of a full membrane microheater indicates the main parts of the power loss at different areas. Inside the cavity and at the top surface heat convection and radiation are present, whereas at the membrane area heat conduction is also considered

considered such as heat convection (P_{conv}) and heat radiation (P_{rad}) (Graf et al. 2007).

Under atmospheric conditions, the heat convection is present both at the top and at the bottom surfaces of the entire membrane as symbolised with the red arrows in Fig. 2. The radiation heat transfer contributes to the thermal loss at over the entire membrane (Fig. 2), but due to the moderate temperatures, it accounts only for a small fraction of the total thermal loss.

In our approach, we divided the total thermal loss into two parts according to Fig. 2. One is the cumulative thermal loss on the surfaces of the active area (at both sides) (P_S), and the other is the thermal loss via the membrane as called membrane loss (P_M). The sum of this two terms is equal to the electric power (P_E) converted to Joule heat by the filament and rises the temperature of the active area uniformly to T Eq. (1)

$$P_E = P_S + P_M \tag{1}$$

This equation describes the power balance of the active area.

For any nth inner ring of the filament the electric power (P_{En}) must be equal with the total thermal loss of the nth segment (P_{Sn}) at their surfaces, as shown in Eq. (2).

$$P_{En} = P_{Sn} \tag{2}$$

In the upper graph of Fig. 2 the height of the hatched columns symbolise the electric power, whereas the orange columns mean the total dissipation capability of the corresponding Inner segments at temperature T.

In case of the outer ring, the membrane heat loss (P_M) must be added to its surface heat loss also (P_{SO}) (Fig. 2), thereby its power consumption (P_{EO}) is written in the form of Eq. (3).

$$P_{EO} = P_{SO} + P_M \tag{3}$$

The total surface thermal loss of the active area (P_S) is expressed as the sum of the surface thermal loss of each segment (P_{Sn}) and outer ring in term of Eq. (4)

$$P_S = P_{SO} + \sum_n P_{Sn} \tag{4}$$

To describe the surface thermal loss capability of the active area we define a temperature dependent heat loss coefficient and call as *total surface thermal loss coefficient*, denoted by $G(\Delta T)$ [W/m^2] or simply G in the equations and in the text. $G(\Delta T)$ means a cumulative surface related heat loss per unit area. This term comprises the effect of all surface related heat loss phenomena (i.e. radiation, convection, heat diffusion) at both sides of the membrane due to temperature difference over the ambient ($\Delta T = T - T_R$). The $G(\Delta T)$ is given as function of temperature difference relative to ambient temperature (T_R). $G(\Delta T)$ is written in

the form of Eq. (5) for an area element A, where P_n is the surface heat loss of the area element at temperature T.

$$G(\Delta T) = \frac{P_n}{A}\bigg|T \tag{5}$$

Consequently, the power dissipation capability of any nth inner segment (P_{Sn}) at temperature T can be expressed as the product of the nth segment area A_{Sn} and G (Eq. 6), and must be equal with the electric power consumed by the filament ring which is running in the segment (P_{En}).

$$P_{En} = P_{Sn} = A_{Sn} \cdot G \tag{6}$$

Following Eq. (1) the power balance of the outer ring is written in the form of Eq. (7)

$$P_{EO} = A_{SO} \cdot G + P_M \tag{7}$$

where A_{SO} is the area of the outer ring.

In view of the microheater electric power utilisation, P_M is useless because it is not dissipated by the active area. In the present design procedure we define a ratio and called *thermal loss ratio $\eta(\Delta T)$*, which expresses a quantitative relation between the surface thermal loss of the active area and the total heat loss of the microheater at temperature T (except the "self heated" feedline heat losses) and described by Eq. (8), wherein further equivalencies were derived using Eq. (1).

$$\eta(\Delta T) = \frac{P_S}{P_M + P_S} = \frac{P_S}{P_E}. \tag{8}$$

Once P_E and $G(\Delta T)$ are determined both $\eta(\Delta T)$, and P_M can be calculated. Although the magnitude of the components of $G(\Delta T)$ are not known quantitatively but the $G(\Delta T)$ value can be approximated by FEM model or can be calculated from the electro-thermal measurements of a *preliminarily fabricated test device* (see in ANNEX D). In the present procedure we chose this latter solution. Based on Eqs. (1–8), analytical equations were derived using the $G(\Delta T)$ and $\eta(\Delta T)$ values for the filament geometry shown in Fig. 1 to find the appropriate sizes of the filament rings. The dimensions of the outer ring as well as the number and the dimensions of the inner rings can be calculated by cubic equations. The methodology is described in detail in Annex A.

3 Design and realization of microhotplate

In this section we demonstrate the realization of the microhotplate via the main five stages of the filament design by exploiting the above theoretical considerations.

3.1 Collecting the input parameters

The input parameters, such as the geometry of the active area, operation conditions, filament material, technology-related data and thermal input parameters are summarized in Table 1. The targeted operation temperature of the circular shaped filament is up to 500 °C which meets the temperature requirement of the overwhelming majority of the high temperature thermo-catalytic sensors (Graf et al. 2007, pp. 45–47) and the needs of the chemo-resistive sensors (Hierlemann 2005, p. 80) as well. The microheater operates in air under ambient pressure (ca. 101 kPa) at room temperature (ca. 25 °C).

In order to facilitate battery-powered operation and to make it compatible with the 3.3 V logic standards the total supply voltage of a single element is 1.5 V.

Due to the chemical stability and the high *TCR*, platinum is selected for the filament material. The electrical properties of the deposited platinum film depend on the material purity, thereby must be measured for the processes used by the foundry. The material constants listed in Table 1 are specified for the layers formed in our laboratory and used in our calculations. According to literature current densities between 1–90 mA/μm^2 are acceptable for platinum thin films when the filament temperature is in the range of $0.3T_m < T < 0.7T_m$, where T_m is the melting point of platinum (1768 °C) (Groenland 2004; Srinivasan et al. 1997; Bondarenko et al. 1955). However, in this design we restricted the current density between 1–10 mA/μm^2 to avoid electro-migration induced resistance drifts.

The filament rings are separated by insulation spacing. Obviously, the smaller the better. In the current design we used 3 μm.

3.2 Design of the outer ring and feedlines

In the second stage the inner radius (r_O) and the current density (J) of the outer ring must be determined by Eqs. (22, 27, 30) described in Annex A using the required parameters from Table 3 (i.e. G, η, ρ_o, v). These terms set the relationship among the supply voltage, current density, layer thickness, width of the outer filament ring, and voltage drop (U) across the filament. Based on the r_O and J values parametrized nomograms can be set as function of supply voltage (U_o) to find the best coincidence between the size of the outer ring, the layer thickness and the current density. Thereof the technical limitations can be properly taken into account.

In our approach this step also fixes the geometric parameters of the supply connections (see in Sect. 2, Annex A).

Table 1 Collected input parameters for filament layout

Description	Abbrev	Quantity	Unit
Geometry of active area			
Circular shaped			
Radius of the active area (see Fig. 1)	r_A	75	μm
Operation circumstances			
Temperature of active area	T	500	°C
Environment: ambient			
Ambient pressure	p	101	kPa
Ambient temperature	T_R	25	°C
Supply voltage at temperature T	U_o	1.5	V
Current density range	J	1–10	mA/μm^2
Filament material: platinum (Pt)			
Pt layer thickness[a]	v	0.4	μm
Specific electrical resistance	ρ_o	113E−3	Ohm μm
Temperature coefficient of resistance	*TCR*	2.8E−3 ± 0.1E−3	1/°C
Technology related parameters			
Insulation spacing (See Fig. 1)	s	3	μm
Thermal parameters			
Total surface thermal loss coefficient at $\Delta T = T - T_R = 475$ °C	$G(\Delta T)$	550E−9	W/μm^2
Thermal loss ratio at $\Delta T = T - T_R = 475$ °C	$\eta(\Delta T)$	0.43	–

[a]Thickness is standard in our laboratory and material constants are valid for layers with the given thickness up to 300 °C

The outer radius of the outer ring (r_A) is equal with the radius of the heated area (Fig. 1), while its inner radius is found as one of the three roots of the cubic equation (Eq. 22, Annex A). The r_O, J, v and the filament voltage drop (U) are coherent values and each of them has to be in their desired range. Thereof J and r_O were calculated for a set of U between 0.8 and 4 V and are plotted as function of U for three different layer thicknesses in a parameterized nomograph (Fig. 3a). Furthermore, once the dimensions of the outer ring are known, then the corresponding total supply voltage (U_o) can be calculated by Eqs. (28)–(30) (see Sect. 2, in the Annex A). The results are interpreted in another parameterized nomograph (Fig. 3b) which reveals the relationships among r_O, J and U_o.

In our design 66.5 μm inner radius of the 400 nm thick platinum was chosen for the outer ring with a calculated width of 8.5 μm. This ring is loaded by ca. $J = 6.1$ mA/μm² current density. The supply voltage is approx. 1.57 V to achieve 500 °C, hence the voltage drop along the filament is around 1.07 V, as indicated in Fig. 3a, b. In this design we selected a higher value for the supply voltage than the targeted one, to have more room if the voltage drop is less along the feedlines than expected. Note that the nomographs in Fig. 3 are valid only for the parameters indicated. If a filament is designed for another operation temperature at the targeted voltage, a new nomograph has to be set up.

According to the rule declared in Sect. 2 in the Annex A, the width of the two feedlines are also 8.5 μm, whereas their length are equal to the half of the mean path length of the outer ring (ca. 222 μm).

3.3 Design of the inner rings

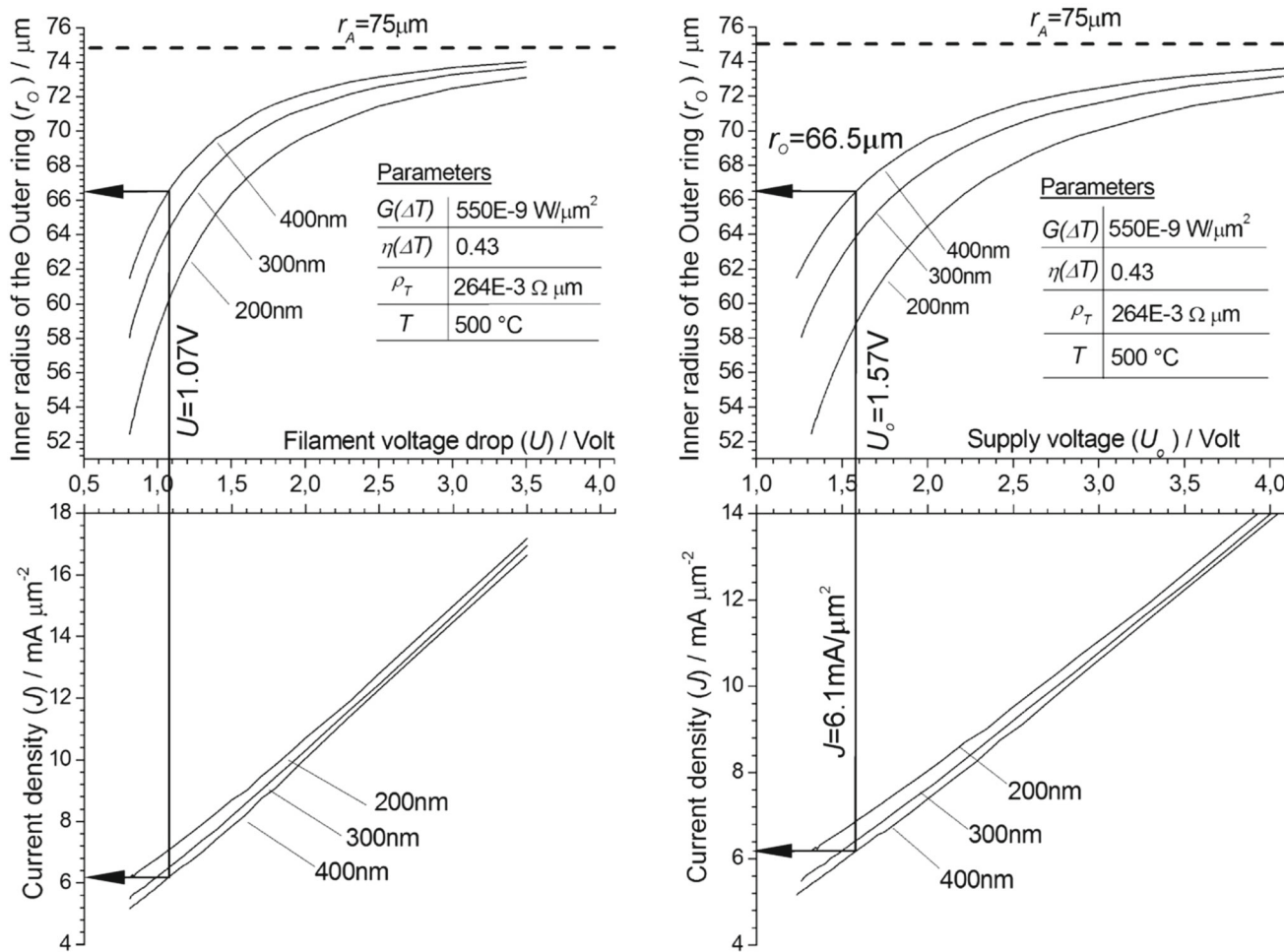The third step is to calculate the radius, the width and the mean path length values of the inner rings. The step-by-

Fig. 3 Parameterized nomographs for 200, 300, 400 nm Pt layer thicknesses are plotted to reveal the relationship among the inner radius of the outer ring (r_O), current density (J) and the supply voltage (U_o). **a** Nomograph indicates the inner radius of the outer filament ring (top) and the current density (bottom) as function of voltage drop along the filament. **b** The same values are indicated as function of supply voltage. Arrows show the results for the 8.5 μm wide outer ring

step calculation is started from the outer ring by applying Eqs. (38–42, Annex A) sequentially. In every sequence the results of the cubic equation returns three roots. Solutions that fulfil the condition are summarized in Table 2. The input parameters and the roots of the cubic equations are tabulated in the flowchart in Annex B. As the third cubic equation solutions didn't result appreciable value, i.e. the radius is larger than the interior area, the third segment of the filament can't be filled with ring. In such a case, an acceptable solution is the filling the remained area with a closed disc. However, the electric power portion of this part of the filament is ca. 1–1.5% of the total power consumption of the active area; one should pay attention to the disc diameter, which may never be smaller than the width of the neighbouring inner ring to avoid the appearance of a hotspot. In the present example, the width of the previous inner ring is 21 μm, whereas the diameter of the available area in the third segment is only 30 μm. Therefore, the third segment is filled with a 30 μm diameter disc.

Finally, the expected electronic performances of the designed filament are listed below:

Supply voltage: 1.5 V.
Supply current: 20.6 mA.
Total power consumption: 31 mW.
Feedline power consumption: 10 mW.
Active area power consumption: 21 mW.

3.4 Filament construction

In the fourth step the whole filament is created by following the steps in Fig. 4. First, the filament rings (except the third one) are sectioned and their parts are connected in series. Preferably, the feedlines should be arranged in opposite position and not advised to connect them directly to the outer ring. It is better to connect them to one of the inner rings through interconnections (Fig. 4c). A plausible solution is illustrated in Fig. 4d. In the present design, the interconnections were placed between the second inner
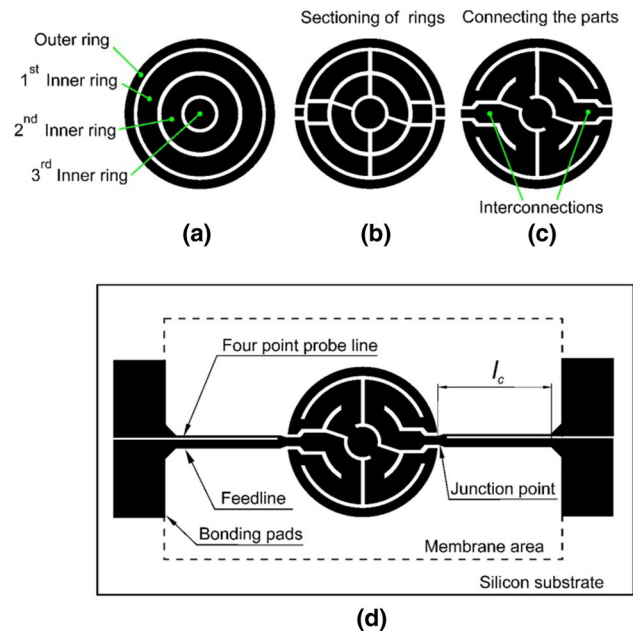

Fig. 4 Steps of the microheater layer generation. **a** Concentric rings with the calculated dimensions are positioned on the heated area. **b** The sectioned rings. **c** Parts are connected in series and interconnections are added to form a contiguous filament. **d** The filament is connected to the bonding pads by feedlines and with the additional connections to four point resistance measurement. The border of the membrane area is indicated by dashed line

ring of filament and feedlines through the junction point, as indicated in Fig. 4c, d.

3.5 Forming the final layout

Finally, the membrane area is determined in the fifth step. One side length of the rectangular shaped membrane is given by the sum of the length of feedlines and the diameter of the active area. It equals with ca. 550 μm. The minimum length of the other side is derived from the minimum distance between the frame of the silicon chip and the heated area. It was calculated by Eq. (9) according to Gall (1991), where d_s is the diameter of the active area,

Table 2 Calculated ring and feedline dimensions in micrometers

Ring	Radius of filament rings				Ring width		Ring mean path length	
Outer ring	Inner radius		Outer radius					
	r_O	66.5	r_A	75	d_O	8.5	l_O	444
Inner rings								
First	r_{1i}	42	r_{1o}	63	d_1	21	l_1	330
Second	r_{2i}	18	r_{2o}	39	d_2	21	l_2	148
Third[a]	r_{3i}	–	r_{3o}	15	d_3	–	l_3	–
Feedline	Feedline width				Feedline length			
	8.5				222			

[a]Third inner ring is a disc

d_m is the minimum diameter of the membrane. In our case d_m is the shorter side length of the rectangle.

$$d_m = 1.64\,d_s \tag{9}$$
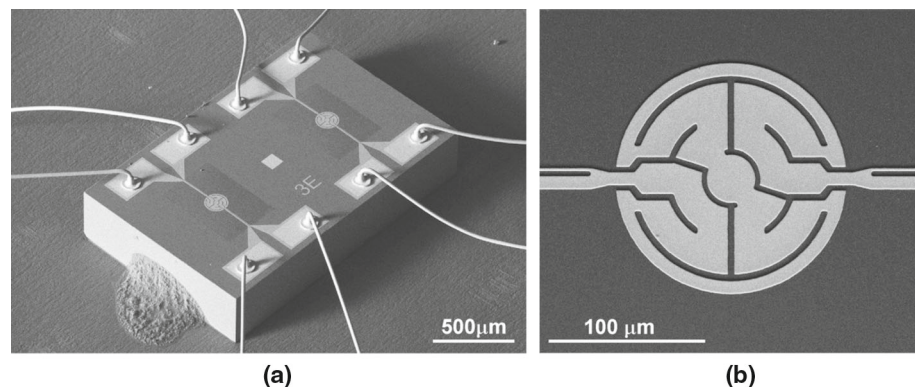
Equation (9) gives d_s = 246 μm wide membrane and minimum 48 μm gap between the outer ring and the silicon frame. In the final design the gap between the active area and silicon frame was increased twice as large as the calculated minimum gap, so the calculated new gap was $2 \times 48 = 96$ μm and the width of the membrane was $150 + 2 \times 96 = 342$ μm. In the final design circa $350 \times 550\,\mu m^2$ membranes were realised for the better heat insulation similarly to *preliminarily fabricated device*.

4 Device fabrication

Full membrane microhotplates were fabricated on 380 μm thick Si wafer (100) using alkaline bulk silicon micromachining for the membrane release. The multilayer membrane structure is set such as to result in a residual stress below 200 MPa. The thermally grown and deposited SiO_2/ Si_3N_4/SiO_2 (400/120/120 nm) multilayer supports the 400 nm thick platinum filament, what is embedded 10–18 nm TiO_x adhesion layer at both sides. Finally, a 300 nm thick SiO_2 layer was deposited to cover the filament. The Pt layer was patterned by RIE instead of the usual lift-off process to avoid spike formations along the side edges of the metal tracks. Finally, KOH anisotropic etching formed the cavities beneath the full membranes.

The processed twin microheater platform is illustrated in scanning electron microscopic images (Fig. 5). The ball bonded chip is mounted onto a PCB. The higher magnification image reveals the characteristic features of the filament sections as well as the feedlines and the connections for the four point resistance measurements. The line width shrinkage due to the wet etching of the aluminium mask layer and platinum dry etching processes was compensated in the photomask design.

5 Temperature measurement by spectral pyrometry

Spectral pyrometry method was used to reveal the temperature of the investigated area. The setup consists of an upright optical microscope (Olympus BX51), where the stage has been replaced by an XYZ piezo stage (Physik Instrumente P-545.3R8S). The microscope is coupled to an aberration corrected imaging spectrograph (Priceton Instruments Isoplane SCT320 with PIXIS 400BRX cooled CCD camera) which allows to record the emission spectra in the 720–980 nm wavelength range. The characterized small spot size is limited by the diffraction phenomena. A dedicated calibration lamp performed wavelength and intensity calibration in this wavelength range.

Mounted chips with suspended filaments were heated by stabilized power supply (Keithley 2400 SourceMeter) and let to stabilize at each supply power under the microscope objective. Twelve characteristic spots (see Fig. 6) were selected at various locations along the filament, and their intensity calibrated spectrum were recorded at each location for five power consumption levels totalling 1340 registered spectral points.

The investigated area in the microscope is estimated to be around 4 μm^2, thereby the values were treated as point sources. Typical series of intensity calibrated emission spectrum collected on spot L are presented in Fig. 7a–c for the five power consumption values (P_E). Similar spectrum were registered at the other spots and analysed in the same manner.

In order to determine the spot temperatures the Wien approximation in the form of Eq. (10) was transformed to obtain Eq. (11)

$$E(\lambda, T) = \epsilon C_1 \lambda^{-5} / \left[exp\left(\frac{C_2}{\lambda T}\right) \right] \tag{10}$$

$$\ln\left(\lambda^5 E\right) = \ln(\varepsilon C_1) - C_2/(\lambda T) \tag{11}$$

Fig. 5 SEM images of a twin filament microhotplate chip. **a** View of the mounted chip. **b** A higher magnification image of the heated area is to illustrate the platinum filament ring architecture
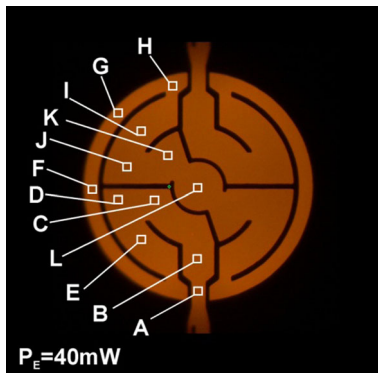
Fig. 6 Spot positions are indicated on the optical image taken from a glowing microfilament. The power consumption of the filament was 40mW

where E is the intensity, C_1 and C_2 are constants ($C_1 = 3.7418 \times 10^{-16}$ W m^2; $C_2 = 0.014388$ m K), T is the temperature, λ is the wavelength.

This approximation is widely used in spectral pyrometry to obtain surface temperatures of different materials (metals and ceramics), filaments (Onnink et al. 2019), and sometimes without using hypothesis about the emissivity (Hagqvist et al. 2013; Magunov 2009; Coates 1981). The Wien law is valid when the $\lambda << C_2/T$ (short wavelength and several hundreds of Kelvin temperature) (Araújo 2017). In practice $5\lambda = C_2/T$ is acceptable (Magunov 2009). As the maximum surface temperature of the filament is around 1100 K, the $\lambda_{max} = 13$ μm which is ca. 13 times higher than the maximum wavelength of our spectral range (980 nm). Consequently, we may use the Wien approximation. The spots are considered as "gray-body" ($\varepsilon(\lambda)$ = constant). The measured spectra are transformed by Eq. (11) in a Cartesian coordinate system, where the ordinate is $\ln(\lambda^5 E)$ and the abscissa is C_2/λ. The temperature can be calculated from the slope of the lines. Even if the emissivity is temperature dependent it only shifts the lines parallel, but their slope remains unchanged. In Fig. 7d the linearized regions of the spectrum are collected with the related fit results, whereas in Fig. 7a–c the calculated temperatures are also indicated. The temperature values are summarised for all the spots in Annex C. Two calculated "gray-body" intensity spectrum (No. 1. and No. 2.) are indicated in Fig. 7a; one for 8 K higher and another for 8 K lower temperatures than the determined 821 °C. The obvious differences reveal that at least ± 1% accuracy is achievable at high temperatures.

The average filament temperature was approximated by the arithmetic mean of the twelve temperature values (T_{AVR}) revealed from the spectral pyrometry measurements for the five power levels. We present these values in Annex C. The temperature deviation (T_{dev}) along the filament was derived as the difference of the T_{AVR} and the spot temperatures. These deviations are plotted in bar diagrams in Fig. 8a–e for the five P_E values.

The resulted temperature deviations are below 3.4% and 0.9% at the average temperatures of 534 and 821.8 °C, respectively. If we accept the results, we may say that spot F, which locates at the outer ring closest to the silicon substrate, shows the lowest temperature at every power level. Temperature of spot A, which locates at the junction point, remains close to the T_{AVR}. This latter indicates that the geometry of the "self heated" feedlines was sufficient to balance their heat conduction effect. The temperature of the other spots showed monotone changing around the T_{AVR} with increasing power level, while the temperature deviation decreases with increasing T_{AVR}.

In view of the 1–3% accuracy limit of the Spectral pyrometry if the wavelength dependency of the emissivity is neglected (Magunov 2009 p. 463; Coates 1981), we may suppose that the absolute temperatures of the spots are within ca. 10–24 °C. Smaller temperature difference can't be distinguished by the present technique, even if the linear fits gave us temperature values with much smaller errors. In this sense, we may regard the temperature deviations in Fig. 8a–e as random error around the T_{AVR}, rather than the accurate temperature non-uniformity of the filament. Note that at higher temperatures with higher intensities the temperature deviations systematically decrease (Fig. 8). This well indicates that the deviations are probable better at lower temperatures than shown by the pyrometry.

6 Electro-thermal performances

We determined the voltage drop along the filament using the four point measurement technique, its power consumption (P_E) and the total power consumption of the microheater (P_{tot}) (latter includes the extra power consumption of "self-heated" feedlines). The measurement was taken on ten randomly chosen devices, and the supply voltage was varied up to 2.7 V. In Fig. 9a the average filament temperature is plotted as function of the filament voltage drop and supply voltage. The average filament temperature was calculated from the measured cold and hot resistances of the filament using the *TCR* of the platinum film in Table 1. Furthermore, we plotted the filament voltage drop and the supply voltage values, which relate to the T_{AVR} temperatures determined by Spectral pyrometry (red circles). In Fig. 9b the average filament temperatures were calculated in the same manner as above and plotted as function of the electric power portions (i.e. P_E, P_{tot}) which were consumed by the filament and the whole microheater. The Spectral pyrometry related average temperature-electric power values are also marked with red circles.
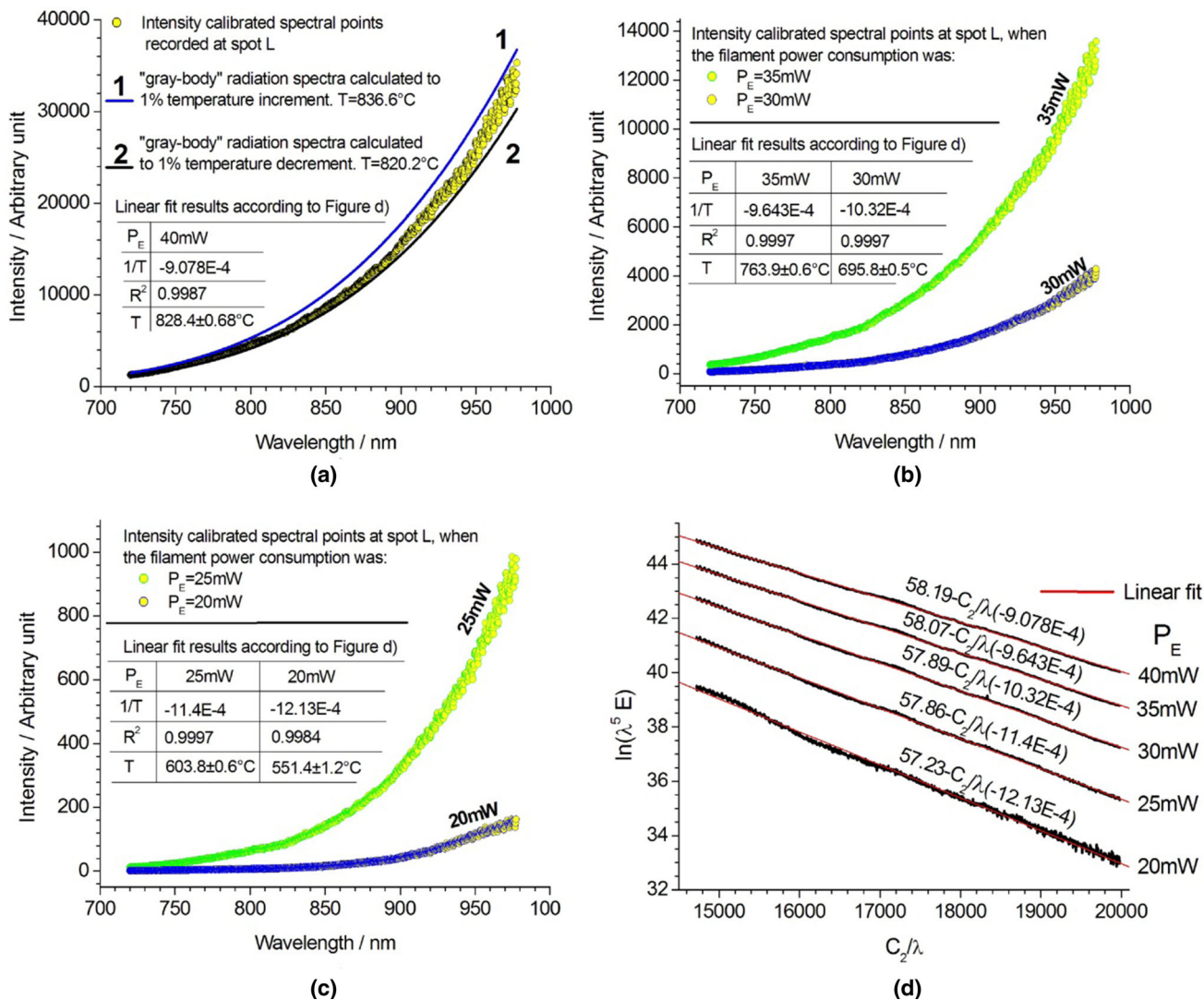
Fig. 7 Typical series of emission spectrum between 720–980 nm wavelengths recorded at spot L for five filament power consumption level (P_E) and their linearized form. **a** The figure indicates a comparison of two calculated "gray-body" radiation curves and the recorded spectral points on spot L to demonstrate the accuracy of the temperature measurement. **b** Two spectrum recorded at 30 and 35 mW power consumption. **c** Spectrum recorded at 25 and 20 mW, close to the sensitivity limit of the pyrometry. **d** Linearized regions of the emission spectrum in the wavelength range of 720–980 nm recorded at spot L for five power consumptions. The indicated linear fits were used to calculate the spot temperatures

According to the *TCR* related calculations the total supply voltage values are varying in 1.4–1.55 V range at 500 °C (Fig. 9a). This temperature was not possible to detect due to the above mentioned limitations of the Spectral pyrometry, but from 534 up to 850 °C both the filament voltage drop and supply voltage values approach quite well the pyromety results. However, they are slightly higher than we revealed from the *TCR* based average calculations (Fig. 9a).

The power consumption values showed similar behaviour. At the same power consumption level of the filament the Spectral pyrometry revealed lower average filament temperature than the corresponding values calculated by

TCR. This difference increases with increasing temperature (Fig. 9b). We think that it can be attributed to the continuous change in the *TCR* of the platinum filament. However, the *TCR* of metal film was characterised with a constant value up to 300 °C, the *TCR* of platinum films decreases slightly with increasing temperature (Kockert et al. 2019; Radetic and Pavlov-Kagadejev 2015; Zhai et al. 2012;).

The self-heated feedlines consume ca. 33% of the total power consumption in the whole range to balance their own heat conduction loss, whilst improve the temperature uniformity of the interconnections and its surroundings. The voltage drop across the feedlines at 500 °C is ca. 0.49–0.54 V, which is very close to the calculated value
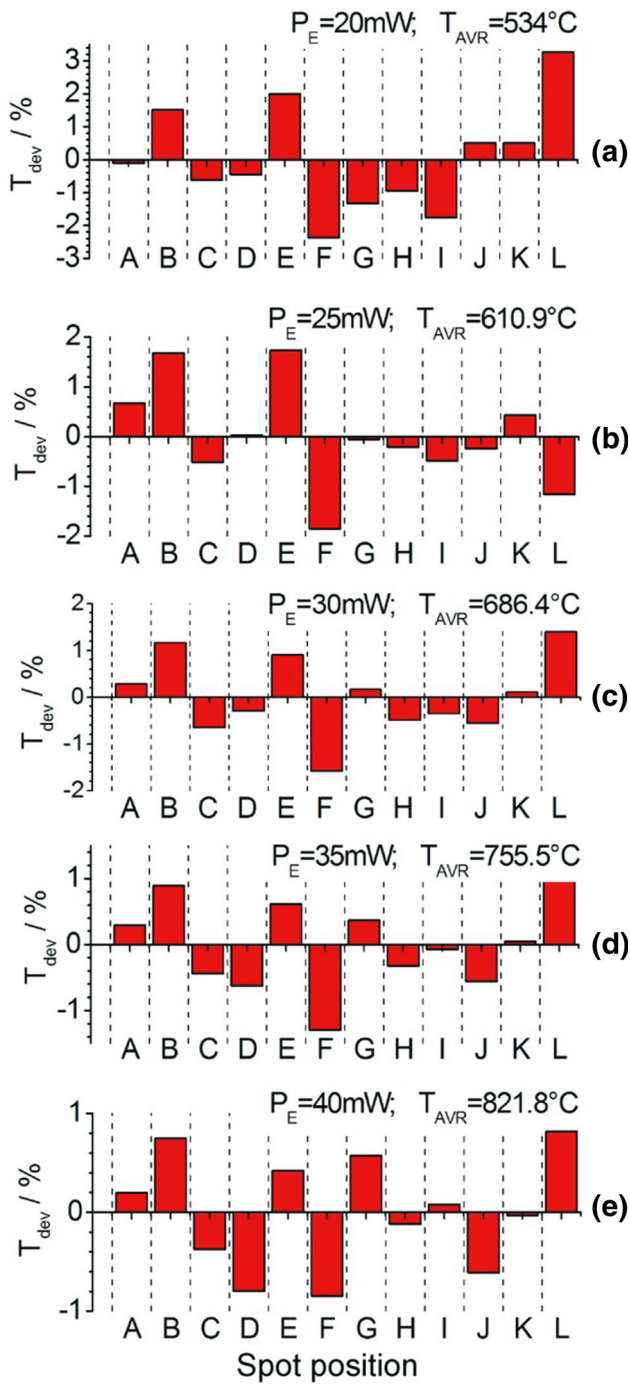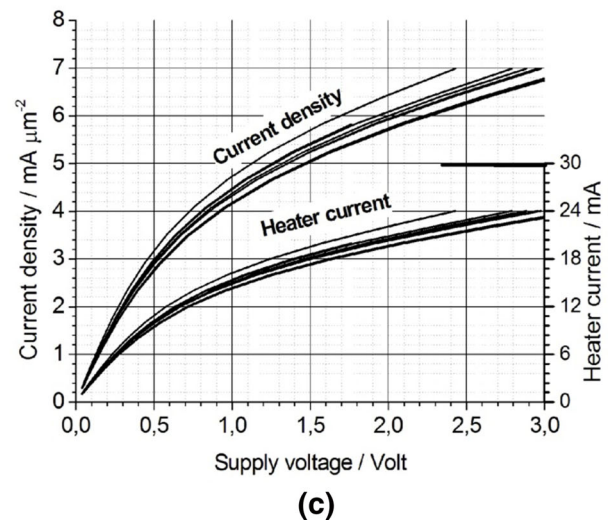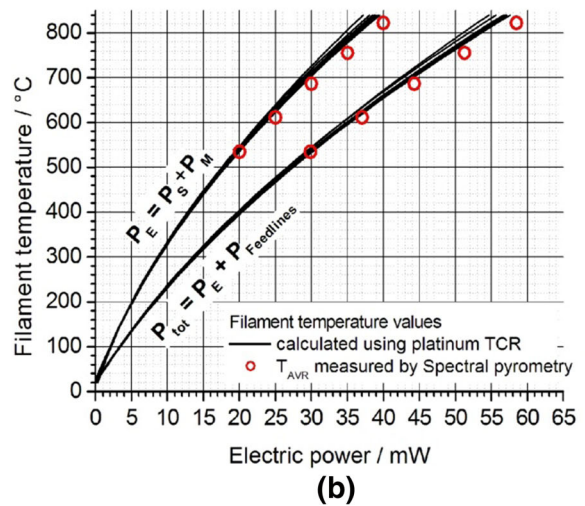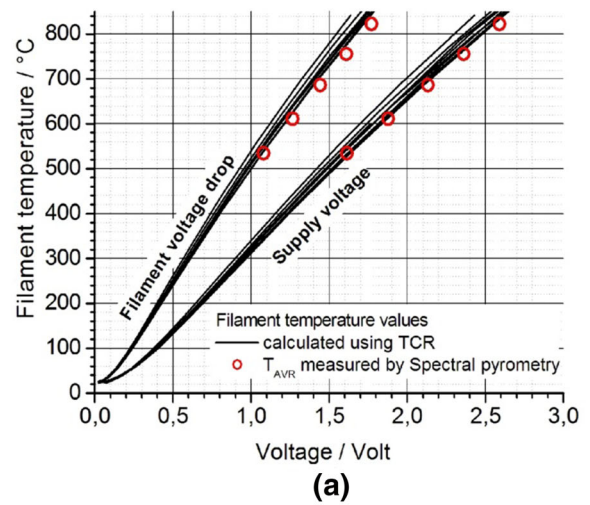
Fig. 8 Spot temperature deviations (T_{dev}) around the average temperature (T_{AVR}) along the filament for the spot positions indicated in Fig. 6 according to the five power consumption values i.e.: **a** 20 mW, **b** 25 mW, **c** 30 mW, **d** 35 mW, **e** 40 mW

◄**Fig. 9** Electro-thermal performances of the microheater. **a** Voltage-filament temperature characteristics show the relationship among the average filament temperature and the filament voltage drop as well as the supply voltage. The temperature values for the continuous black line curves were calculated using the *TCR* of the platinum film in Table 1. The average filament temperatures (T_{AVR}) as determined by spectral pyrometry are also indicated. **b** Average filament temperature as function of the power consumption of the filament (P_E) and the total power consumption (P_{tot}). **c** Calculated current density in the outer ring and the measured heater current curves as function of supply voltage, both values meet the requirements

when applying a linear temperature drop along the feedlines (see Sect. 2 in ANNEX A).

The total power consumption and the filament power consumption at 500 °C are slightly lower than estimated (Fig. 9b). This is the consequence of the overestimated G value and underestimated η in Table 3. The reason is the differences between the preliminarily set conditions, i.e. instead of $G(475\ °C) = 550 \times 10^{-9}\ \mathrm{W/\mu m^2}$ and $\eta(475\ °C) = 0.43$, $G(475\ °C) = 450 \times 10^{-9}\ \mathrm{W/\mu m^2}$ and $\eta(475\ °C) = 0.45$ were found for the fabricated microhotplate (see in ANNEX D).

7 Conclusions

A simplified analytical method was developed to design annular single-filament microhotplates with uniform surface temperature. Beyond the thermal performance, the model enables to consider all the important parameters defined by the device operation conditions and the processing technology. The thermal properties of the processed hotplates were analysed by electro-thermal measurements and optical pyrometry. Temperature uniformity of $\pm 3.5\%$ to $\pm 1\%$ was obtained when the temperature was stepwise increased from 530 and to 830 °C, respectively. Considering the poor reliability of the pyrometric method at lower temperatures we assume that the $\pm 1\%$ inhomogeneity is achieved in the full temperature range investigated. As most of the sensors require uniform operation temperature, the presented methodology enables to operate this essential component without the need for complex driving circuit.

Annex A

Relationships supporting the filament geometry design

Equations (1–8) will be referred to the main text.

Geometry of the outer filament ring

In the presented design procedure, the shape of the active area is circular and its radius (r_A) is set as prerequisite. Since the same current flows in all of the filament rings (I), the electric power consumed by the outer ring can be expressed as function of the voltage drop along the filament (U) in the following manner:

The electric power consumption of the filament (P_E) (except feedlines) equals to the product of the voltage drop along the filament (U) and heater current which flows through thereof Eq. (12)

$$P_E = U \cdot I \tag{12}$$

Combining Eq. (8) and Eq. (12) the heater current is written in the form of Eq. (13)

$$I = \frac{P_E}{U} = \frac{P_S}{U \cdot \eta} \tag{13}$$

Expressing P_S by means of G for the area of the active area using Eq. (5) and substituting it into Eq. (13), the filament current is written in the form of Eq. (14)

$$I = \frac{G \cdot \pi \cdot r_A^2}{\eta \cdot U} \tag{14}$$

Using the outer ring dimensions (Fig. 1), the electric power consumption of the outer ring (P_{EO}) is given by Eq. (15)

$$P_{EO} = I^2 \cdot \frac{\rho_T \cdot l_O}{v \cdot d_O} = \frac{G^2 \cdot \pi^2 \cdot r_A^4 \cdot \rho_T \cdot l_O}{\eta^2 \cdot U^2 \cdot v \cdot d_O} \tag{15}$$

where v is the filament metal layer thickness, d_O is the width of outer ring, l_O the mean path length of the outer ring, ρ_T is the specific electrical resistance of the filament material at the required operation temperature T. Here the Temperature Coefficient of Resistance (*TCR*) of the filament material has to be considered according to Eq. (16)

$$\rho_T = \rho_o \cdot [1 + TCR \cdot (T - T_R)] \tag{16}$$

where ρ_o is the specific electrical resistance of the filament material at room temperature (T_R).

The surface thermal loss of the outer ring (P_{SO}) at temperature T is calculated by Eq. (17) using G and the filament dimensions

$$P_{SO} = G \cdot \pi \cdot (r_A^2 - r_O^2) \tag{17}$$

where r_O is the inner radius of the outer ring.

Expressing the total surface loss of the active area by Eq. (5) and combining with Eq. (8), the membrane thermal loss is described by Eq. (18)

$$P_M = P_S \cdot \frac{1 - \eta}{\eta} = \frac{G \cdot r_A^2 \cdot \pi \cdot (1 - \eta)}{\eta} \tag{18}$$

Substituting Eqs. (15), (17), (18) into power balance equation of the outer ring Eq. (3) and considering that the outer ring width is

$$d_O = r_A - r_O \tag{19}$$

outer ring mean path length is

$$l_p = (r_A + r_O) \cdot \pi \tag{20}$$

the term of Eq. (21) is resulted

$$G \cdot \pi \cdot (r_A^2 - r_O^2) + \frac{G \cdot r_A^2 \cdot \pi \cdot (1 - \eta)}{\eta}$$
$$= \frac{G^2 \cdot \pi^3 \cdot r_A^4 \cdot (r_A + r_O) \cdot \rho_T}{\eta^2 \cdot U^2 \cdot v \cdot (r_A - r_O)} \tag{21}$$

Carrying out the multiplications in equation Eq. (21) and sorting the terms to the left side, the cubic equation Eq. (22) is given:

$$X - Y \cdot r_O - W \cdot r_O^2 + Z \cdot r_O^3 = 0 \tag{22}$$

where X, Y, W, Z coefficients are

$$X = \eta \cdot U^2 \cdot v \cdot r_A^2 - G \cdot \pi^2 \cdot r_A^5 \cdot \rho_T \tag{23}$$

$$Y = \eta \cdot U^2 \cdot v \cdot r_A^2 + G \cdot \pi^2 \cdot r_A^4 \cdot \rho_T \tag{24}$$

$$W = \eta^2 \cdot U^2 \cdot v \cdot r_A \tag{25}$$

$$Z = \eta^2 \cdot U^2 \cdot v \tag{26}$$

Note that, all physical quantities except r_O (inner radius of the outer filament) are known or can be specified in Eq. (22). The equation returns three solutions. The one which satisfies the condition: r_O is real number and $0 < r_O < r_A$, that will be the inner radius of the outer ring (r_O).

The magnitude of the current density is another important quantity of the microfilaments. Due to the material specific properties, it must be limited such as not to exceed the permissible current density specified for the filament material in order to avoid the electromigration related resistance drift. Combining Eq. (14) with the outer ring cross section ($d_o \bullet v$) the current density in outer ring can be expressed as function of the voltage drop along the filament as Eq. (27)

$$J = \frac{G \cdot \pi \cdot r_A^2}{\eta \cdot U \cdot d_O \cdot v}. \tag{27}$$

Feedline geometry and supply voltage calculation

Filaments are powered through feedlines that fabricated from the metal layer of the filament. In practice, micro-heaters require nominal supply voltage to reach the operation temperature. The supply voltage divides across the feedlines and the filament. Moreover, due to its good heat dissipative capability, the feedline geometry also affects the temperature distribution of the active area. In practice, the feedlines are designed as a trade-off among the acceptable extra power consumption, the temperature uniformity at the active area and the electromigration related maximum current density.

Once the outer ring dimension and the current density are fixed, the feedline dimensions and the total supply voltage can be determined. Based on our experience to create a so called "self-heated" feedline, we can make the following statement for the present architecture: the feedline width has to be equal to the width of the outer ring when the feedline length is equal to the half of the mean path length of the outer ring ($l_O/2$). This approach ensures an almost unaffected temperature distribution along the active area, but on the other hand, it manifests in extra power consumption. In this case, an approximately linear temperature drop along the feedline is considered to estimate the voltage drop so the average temperature of it (T_T) is explained by Eq. (28), whilst the voltage drop across the feedline is determined by Eq. (29)

$$T_T = \frac{T - T_R}{2} \tag{28}$$

$$U_T = \frac{\rho_o \cdot [1 + TCR \cdot (T_T - T_R)] \cdot l_O \cdot J}{2} \tag{29}$$

where Eq. (16) is used. The current density in the feedlines is equal with current density in the outer ring, so the total supply voltage (U_o) can be determined by Eq. (30)

$$U_o = 2 \cdot U_T + U \tag{30}$$

Geometry of the inner filament rings

The design of the inner ring requires an insulation distance (s) which is limited by the available lithographic resolution and the filament fabrication technology (Fig. 1). Obviously, the same current flows in every ring and there are no bypasses and current leaks.

Combining the defined equations Eq. (5) and Eq. (6) the term of Eq. (31) is derived

$$P_{Sn} = G \cdot A_{Sn} = G \cdot \pi \cdot (r_{no}^2 - r_{ni}^2) \tag{31}$$

where P_{Sn} is the surface thermal loss of the nth inner segment, r_{no} is the outer radius, r_{ni} is the inner radius of the nth inner segment (see Fig. 1).

The electric power consumed by the $n.^{th}$ inner filament ring (P_{En}) is expressed by Eq. (32)

$$P_{En} = R_{ni} \cdot I^2 = \rho_T \cdot \frac{l_{ni}}{d_{ni} \cdot v} \cdot I^2 = \frac{l_{ni}}{d_{ni}} \cdot J^2 \cdot d_O^2 \cdot v \cdot \rho_T \tag{32}$$

In Eq. (32) the following equations were used:

– the heater current (I) Eq. (33), expressed by the current density (J) as set for the outer ring by Eq. (27)

$$I = J \cdot d_O \cdot v \tag{33}$$

– the mean path length of the inner ring (l_{ni}) Eq. (34)

$$l_{ni} = (r_{no} + r_{ni} - s) \cdot \pi \tag{34}$$

and the inner ring width (d_{ni}) Eq. (35)

$$d_{ni} = r_{no} - r_{ni} - s \tag{35}$$

Furthermore, the $J^2 \cdot d_O^2 \cdot \rho_T \cdot v$ in Eq. (32) is constant for the microheater at the operation temperature T and we denote with C

$$C = J^2 \cdot d_O^2 \cdot \rho_T \cdot v \tag{36}$$

Making Eqs. (31) and (32) equal and substituting Eqs. (34), (35), (36) into Eq. (22) the Eq. (37) is resulted

$$G \cdot \pi \cdot \left(r_{no}^2 - r_{ni}^2\right) = \frac{(r_{ni} + r_{no} - s) \cdot \pi \cdot C}{r_{no} - r_{ni} - s} \tag{37}$$

Carrying out the multiplications in Eq. (37) and sorting the terms to left side, the Eq. (38) cubic equation is written:

$$X \cdot r_{ni}^3 - Y \cdot r_{ni}^2 - W \cdot r_{ni} + Z = 0 \tag{38}$$

where the X, Y, W, Z coefficients are expressed in Eqs. (39)–(42)

$$X = G \tag{39}$$

$$Y = G \cdot (r_{no} - s) \tag{40}$$

$$W = G \cdot r_{no}^2 + C \tag{41}$$

$$Z = G \cdot \left(r_{no}^3 - s \cdot r_{no}^2\right) - C \cdot (r_{no} - s) \tag{42}$$

Since r_{no} is known for the first segment, because it is equal to the inner radius of the outer ring (r_O). For the second and higher rank inner segments the r_{no} is equal to the inner radius of the previously (n-1) calculated segment ($r_{no} = r_{n-1i}$) (see Fig. 1). The s is the insulation distance between the filament rings, what is chosen by the designer, the C constant and G are also known at the desired operation temperature T. Thereby, only the inner radius of the nth segment (r_{ni}) is unknown in Eq. (38).

Solving the cubic equation, it returns three solutions. One of the solutions which satisfies the condition: r_{ni} is a real number and $0 < r_{ni} < r_{no}$, will be the required inner radius (r_{ni}) for both the inner segment and the inner filament ring inside. The cubic equation is repeated until it returns interpretable result in the solutions. Number of the right solutions is equal to the number of inner rings, which will build up the filament at the interior of the active area. The width of the nth inner ring is calculated by the Eq. (35).

Annex B

Tables 3, 4, and 5 below summarise the input parameters and results of segment and ring dimensions.

Table 3 First segment

Input parameters	$r_{lo}=r_O=66.5\mu m$	C=294E-6 (W)		$G(\Delta T)$=550E-9 (W/ μm²)	
Cubic equation	**Coefficients**				
	X	Y	W	Z	
	0.55	34.87	2718.9	135101	
	Roots (r_{li})				
		I.	II.	III.	
		~~-66.49~~	42.05	~~87.84~~	
Condition: r_{ni}: real number; $0<r_{ni}<r_{no}$					
Final dimensions	1st Segment	r_{li}	42 μm	*rounded value*	
	1st Inner ring	d_{li}	21 μm		

Table 4 Second segment

Input parameters	$r_{2o} = r_{1i} = 42 \mu m$		$C = 294E\text{-}6$ (W)	$G(\Delta T) = 550E\text{-}9$ (W/ μm^2)	
Cubic equation	**Coefficients**				
	X	Y	W	Z	
	0.55	21.45	1264.2	26371	
	Roots (r_{2i})				
		I.	II.	III.	
		~~-42.2~~	17.9	~~63.3~~	
	Condition: r_{ni}: real number; $0 < r_{ni} < r_{no}$				
Final	2nd Segment	r_{2i}		18 μm	*rounded value*

Table 5 Third segment

Input parameters	$r_{3o} = r_{2i} = 18 \mu m$		$C = 294E\text{-}6$(W)	$G(\Delta T) = 550E\text{-}9$ (W/ μm^2)	
Cubic equation	**Coefficients**				
	X	Y	W	Z	
	0.55	8.25	472.2	-1737	
	Roots (r_{3i})				
		I.	II.	III.	
		~~-20.01~~	-4.04	~~39.05~~	
	Condition: r_{ni}: real number; $0 < r_{ni} < r_{no}$				
Final dimensions	3rd Segment	r_{3i}		-	*no solution*
	3rd Inner ring	d_{3i}		-	*no solution*

Notation: Pay attention to the sign of the coefficients in Eq. (38) when solving the cubic equation.

Roots of the third cubic equation are fail the condition, so there is no enough room for forming the ring with appropriate dimension. In this case the remained area is filled with a disc of 15 μm radius.

Annex C

See Table 6.

Table 6 Summary of spot temperatures measured on the designed microfilament by Spectral pyrometry for the dedicated five heating power values (P_E)

P_E/mW	Temperature/°C				
	40	35	30	25	20
Spot temperatures					
A	823.4 ± 0.6	757.7 ± 0.5	688.3 ± 0.5	615.0 ± 0.5	533.4 ± 1
B	827.9 ± 0.6	762.2 ± 0.5	694.3 ± 0.4	621.1 ± 0.5	542 ± 1.1
C	818.7 ± 0.6	752.1 ± 0.5	681.9 ± 0.5	607.7 ± 0.4	530.7 ± 1
D	815.2 ± 0.6	750.7 ± 0.5	684.3 ± 0.5	611 ± 0.5	531.6 ± 1.1
E	825.2 ± 0.6	760.1 ± 0.5	692.6 ± 0.5	621.4 ± 0.5	544.6 ± 1.1
F	814.8 ± 0.6	745.7 ± 0.5	675.4 ± 0.4	599.6 ± 0.4	521.3 ± 1.1
G	826.5 ± 0.6	758.2 ± 0.5	687.5 ± 0.4	610.5 ± 0.4	526.8 ± 1.1
H	820.8 ± 0.6	753 ± 0.5	683 ± 0.5	609.6 ± 0.6	528.9 ± 1.1
I	822.4 ± 0.6	754.9 ± 0.5	683.9 ± 0.4	607.9 ± 0.4	524.6 ± 1
J	816.7 ± 0.6	751.2 ± 0.5	682.5 ± 0.5	609.4 ± 0.5	536.7 ± 1
K	821.5 ± 0.6	755.8 ± 0.5	687.1 ± 0.5	613.5 ± 0.5	536.7 ± 1.1
L	828.5 ± 0.6	763.9 ± 0.5	695.9 ± 0.5	603.8 ± 0.5	551.4 ± 1.2
T_{AVR}/°C	821.8	755.5	686.4	610.9	534

The T_{AVR} means the mean values of the spot temperatures for the each dedicated power level

Annex D

(i) Preliminarily fabricated device.

Figure 10 illustrates the structure of the *preliminarily fabricated device* used to determine the starting values of G and η for the design procedure. The active area diameter was 150 μm. The membrane structure and size were similar to that of the designed microheater described in the main text.

(ii) Determination procedure of $G(\Delta T)$ value

For example, in this section authors describe the method which was used to calculate the *total surface thermal loss coefficient* of the designed microheater. We note, the $G(475)$ value (see Table 1 in the main text) was approximated in a similar manner for the *preliminarily fabricated device* too using its own filament dimensions and material constants.

To calculate the G experimentally, we use the measured dimensions of the inner segments and inner filament rings, the average temperature of the filaments rings, heater current values and filament material constants. We note, due to the etching process, these measured dimensions show a few micron deviation compared to the targeted size. Based on these values the electric power dissipation for each inner ring can be calculated. Dividing the electric power value with the segment area we get the individual G_i values for every inner segment. The average of these G_i values results the *total surface thermal loss coefficient* $G(\Delta T)$ at the given active area temperature.

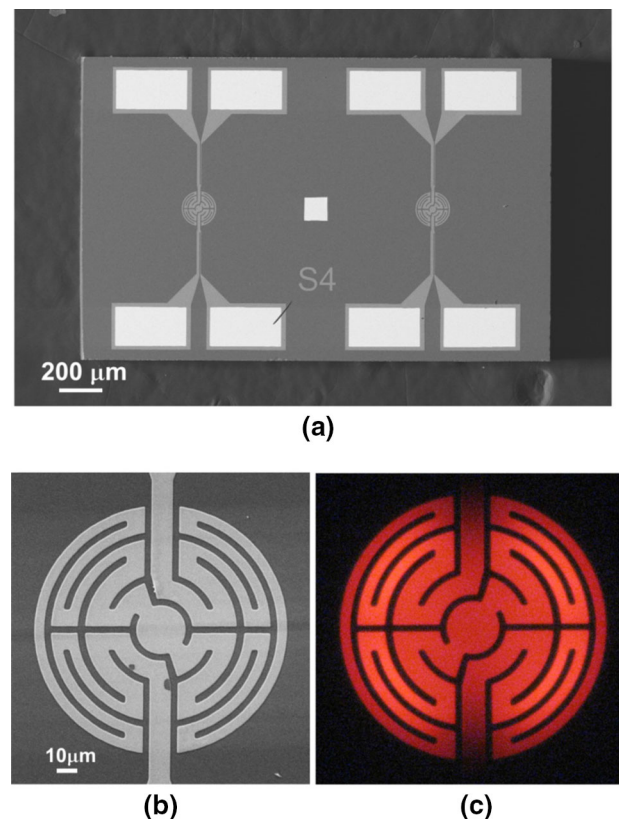Using the filament material constants in Table 1, the measured filament dimensions of a realised device, and the

(a)

(b)   (c)

Fig. 10 *Preliminarily fabricated device*. **a** SEM image of the twin micro-heater. **b** Large magnification of the active area. **c** Optical photo of the filament under operation. The filament power consumption was 40 mW

heater current at 500 °C, the $G(\Delta T)$ values were calculated for the two inner filament rings. The area of the first segment was found to $A_1 = 7606 \mu m^2$, the filament power

consumption of the first segment was c.c. P_{E1} = 3.52mW, calculated by Eq. (32). Applying Eq. (5) to the first segment its *total surface thermal loss coefficient* is G_1 (475 °C) = P_{E1}/A_1 = 462 × 10^{-9} W/μm². This value for the second segment was G_2(475 °C) = P_{E2}/A_2 = 438 × 10^{-9} W/μm². The mean value of these former two G values is G(475 °C) = 450 × 10^{-9} W/μm² ± 2.6%. We note, the difference between the calculated G_1 and G_2 values is low, but due to the accuracy of the filament size measurement method and line width deviations the relative error of the calculated G (ΔT) value is around 10–15%.

Declarations

Conflict of interest The authors declare no conflicts of interest of any kind.

References

Ali SZ, Santra S, Haneef I, Schwandt C, Kumar RV, Milne WI, Udrea F, Guha PK, Covington JA, Gardner JW, Garofalo V (2009) Nanowire hydrogen sensor employing CMOS microhotplate. Sensors 2009:114–117. https://doi.org/10.1109/SENSORS14945.2009

Araújo A (2017) Multi-spectral pyrometry—a review. Meas Sci Technol 28:082002. https://doi.org/10.1088/1361-6501/aa7b4b

Bondarenko VV, Kvartskhava IF, Pliutto AA, Chernov AA (1955) Resistance of metals at high current densities. Sov Phys JEPT 1(2)

Briand D, Krauss A, Schoot A, Weimar U, Barsan N, Göpel W, de Rooji NF (2000) Design and fabrication of high-temperature microhotplates for drop-coated gas sensor. Sens Actuators B Chem 68:223–233. https://doi.org/10.1016/S0925-4005(00)00433-0

Coates PB (1981) Multi-wavelength pyrometry. Metrologia 17(3):103. https://doi.org/10.1088/0026-1394/17/3/006

Dibbern U (1990) A substrate for thin-film gas sensors in microelectronic technology. Sens Actuators B Chem 2:63–70. https://doi.org/10.1016/0925-4005(90)80010-W

Gall M (1991) The Si planar pellistor: a low power pellistor sensor is Si thin film technology. Sens Actuators B Chem 4:533–538. https://doi.org/10.1016/0925-4005(91)80165-G

Graf M, Barrettino D, Baltes HP, Hierlemann A (2007) CMOS hotplate chemical microsensor. Springer-Verlag, Berlin

Groenland AW (2004) Degradation processes for platinum thin films on a silicon nitride surface. Essay (Bachelor) University of Twente

Hagqvist P, Sikström F, Christiansson AK (2013) Emissivity estimation for high temperature radiation pyrometry on Ti–6Al–4V. Measurement 46(2):871–880. https://doi.org/10.1016/j.measurement.2012.10.019

Hartman T, Geitenbeek RG, Wondergem SC, Stam W, Weckhuysen BM (2021) *Operando* nanoscale sensors in catalysis: all eyes on catalyst particles. ACS Nano 14(4):3725–3735. https://doi.org/10.1021/acsnano.9b09834

Hierlemann A (2005) Integrated chemical microsensor systems in CMOS technology. Springer-Verlag, Berlin

Hille P, Strack H (1992) A heated membrane for a capacitive gas sensor. Sens Actuators A 33:321–325. https://doi.org/10.1016/0924-4247(92)80006-O

Hotovy I, Rehacek V, Mika F, Lalinsky T, Hascik S, Vanko G, Drzik M (2008) Gallium arsenide suspended microheater for MEMS sensor arrays. Microsyst Technol 14:629–635. https://doi.org/10.1007/s00542-007-0470-6

Ishaku LA, Hutson D, Gibson D (2021) Development of a MEMS hotplate based MEMS based photoacoustic CO_2 sensor. J Measurement Eng 2(9):95–105. https://doi.org/10.21595/jme.2021.21852

Ishihara H, Masuno K, Ishii M, Kumagai S, Sasaki M (2017) Enhanced plasmonic wavelength selective infrared emission combined with microheater. Materials 10(9):1085. https://doi.org/10.3390/ma10091085

Khan U, Falconi C (2013) Temperature distribution in membrane-type microhotplates with circular geometry. Sens Actuators B Chem 117:535–542. https://doi.org/10.1016/j.snb.2012.11.007

Khan U, Falconi C (2014) An accurate and computationally efficient model for membrane-type circular-symmetric microhotplates. Sensors 14:7374–7393. https://doi.org/10.3390/s140407374

Kockert M, Mitdank R, Zykov A, Kowarik S, Fischer SF (2019) Absolute Seebeck coefficient of thin platinum films. J Appl Phys 126:105106. https://doi.org/10.1063/1.5101028

Kuo JTW, Yu L, Meng E (2012) Micromachined thermal flow sensors—a review. Micromachines 3:550–573. https://doi.org/10.3390/mi3030550

Lee J, King JWP (2007) Microcantilever hotplates: design, fabrication and characterisation. Sens Actuators A 136:291–298. https://doi.org/10.1016/j.sna.2006.10.051

Lochbaum A, Fedoryschyn Y, Dorodnyy A, Koch U, Hafner C, Leuthold J (2017) On-chip narrow band thermal emitter for mid-IR optical gas sensing. ACS Photon 4(6):1371–1380. https://doi.org/10.1021/acsphotonics.6b01025

Magunov AN (2009) Spectral pyrometry (review). Instrum Exp Techn 52(4):451–472. https://doi.org/10.1134/S0020441209040010

Marconot O, Juneau-Fecteau A, Fréchette LG (2021) Toward applications of near-field radiative heat transfer with microhotplates. Sci Rep 11:14347. https://doi.org/10.1038/s41598-021-93695-7

Mele L, Konings S, Dona P, Evertz F, Mitterbauer C, Faber P, Schampers R, Jinschek JR (2016) A MEMS-based heating holder for the direct imaging of the simultaneous *in-situ* heating and biasing experiments in scanning/transmission electron microscopes. Microsc Res Tech 79:239–250. https://doi.org/10.1002/jemt.22623

Nuscheler F (1986) A silicon gas sensor to detect combustible gases. In: 2nd int. meet. chem. sensors, Bordeaux, France, July 7–10, pp 235–238

Onnink AJ, Schmitz J, Kovalgin A (2019) How hot is the wire: optical, electrical and combined methods to determine filament temperature. Thin Solid Films 674:22–32. https://doi.org/10.1016/j.tsf.2019.02.003

Popa D, Udrea F (2019) Towards Integrated mid-Infrared Gas Sensors. Sensors 19(9):2076. https://doi.org/10.3390/s19092076

Queen DR, Hellman F (2009) Thin film nanocalorimeter for heat capacity measurements of 30 nm film. Rev Sci Instrum 80:063901. https://doi.org/10.1063/1.3142463

Radetic RM, Pavlov-Kagadejev M (2015) Analog linearization of Pt100 working characteristics. Serb J Electr Eng 12(3):345–357. https://doi.org/10.2298/SJEE1503345R

Roslyakov IV, Kolesnik IV, Evdokimov PV, Skryabina OV, Garshev AV, Mironov SM, Stolyarov VS, Baranchikov AE, Napolskii KS (2021) Microhotplate catalytic sensor based on porous alumina: *Operando* study of methane response hysteresis. Sens Actuators B Chem 330:129307. https://doi.org/10.1016/j.snb.2020.129307

Rüffer D, Hoehne F, Bühler J (2018) New digital metal-oxide (MOx) sensor platform. Sensors 18(4):1052. https://doi.org/10.3390/s18041052

Srinivasan R, Hsing IM, Berger PE, Jensen KF, Firebaugh SL, Schmidt MA, Harold MP, Lerou JJ, Ryley JF (1997) Microfabricated reactors for catalytic partial oxidation reactions. AIChE J 43:3059–3069. https://doi.org/10.1002/aic.690431117

VanHorn A, Zhou W (2016) Design and optimisation of a high temperature microheater for ink jet deposition. Int J Adv Manuf Technol 86:3101–3111. https://doi.org/10.1007/s00170-016-8440-8

Vauchier C, Charlot D, Delapierre G (1991) Thin-film gas catalytic microsensors. Sens Actuators B Chem 5:33–36. https://doi.org/10.1016/0925-4005(91)80216-7

White R (2014) The pellistor is dead? Long live the pellistor! https://www.envirotech-online.com/article/environmental-laboratory/7/sgx-sensortech/the-pellistor-is-dead-nbsplong-live-the-pellistor/1699

Wu Y, Du X, Li Y, Tai H, Su Y (2019) Optimisation of temperature uniformity of a serpentine thin film heater by a two dimensional approach. Microsyst Technol 25(1):69–82. https://doi.org/10.1007/s00542-018-3932-0

Yunusa Z, Hamidon MN, Kaiser A, Awang Z (2014) Gas sensors: a review. Sens Transducers 168(4):61–75

Zhai Y, Cai C, Huang J, Liu H, Zhou S, Liu W (2012) Study on Pt resistance characteristics of Pt thin film. Phys Proc 32:772–778. https://doi.org/10.1016/j.phpro.2012.03.634